Chemical Engineering Journal 514 (2025) 163164

Contents lists available at ScienceDirect

Chemical Engineering Journal

journal homepage: www.elsevier.com/locate/cej

Determining the kinetic of the oxidation of metallic solid particles☆

Benedetta A. De Liso [a], Gianmaria Pio [a], Clément Chanut [b], Ernesto Salzano [a,*]

[a] Department of Civil, Chemical, Environmental, and Materials Engineering – University of Bologna, Bologna, Italy
[b] Laboratoire des Sciences des Risques, IMT Mines Alès, Alès, France

ARTICLE INFO

Keywords:
Iron
Kinetic Mechanism
Oxidation
Energy production
Heterogeneous reactions

ABSTRACT

The use of non-nano iron particles is currently under investigation for several industrial applications, including carbon-free power production. Nevertheless, poor understanding from the fundamental point of view has been reached on the phenomena ruling the oxidation, with detrimental effects on the performance and safety of reactive systems. In this perspective, this work presents an experimental campaign investigating the oxidation of iron particles in a quiescent regime, exposed to external heat fluxes. Different boundary conditions were explored to this scope, monitoring the sample mass and heat release rate along with the tests. The acquired measurements were integrated with Scanning Electron Microscopy analyses. A mechanicistic model identifying the production of *FeO*, Fe_3O_4, and Fe_2O_3 was proposed and corroborated by the comparison of the collected data, showing excellent agreement between the enthalpy of reactions deriving from experiments and literature. The variations in oxidized structures lead to a regime ruled by intraparticle diffusion of oxygen, once large diameters are explored. The investigation of the kinetic and ignitability of iron powder allows for a technical-based approach for a proper, optimized, and safe design of reactive and storing systems involving iron and iron oxide particles, debottlenecking their use at industrial scales.

1. Introduction

The combination of strength, workability, and durability has largely promoted the use of metals in different human activities over the centuries. Among others, iron powder plays an essential role in the chemical and process industries, also because of its utilization within the ammonia economy [1], wastewater treatment [2], and pyrolysis of mixed plastics [3]. However, only recently, the role of iron within the energy transition has been indicated as a promising route. Indeed, metallic iron is considered a candidate for future renewable energetic production, as an aero-space propellant [4], as well as a carbon-free energy carrier [5]. The latter approach is based on the concept of circular energy economy, where renewable-based energy is adopted to produce hydrogen, which is used to reduce iron oxide powder, making the transportation of energy carriers safer and allowing for energy release in iron-fired power plants [6]. This strategy has the intrinsic advantage of enabling the retrofitting of existing power plants and infrastructures [3], with obvious implications from the economic point of view and on the feasibility of its implementation. In this view, an in-depth knowledge of the chemistry of the iron powder is paramount either during the reduction or oxidation stages [7]. Similarly, once oxidized, iron particles can be also employed as an oxygen carrier, allowing for the implementation of chemical looping strategies in different industrial fields, as reported in dedicated literature reviews [8910]. Besides, the use of pure iron as a renewable energetic material, in the Direct Reduction Iron (DRI) process (sponge iron) [11] for sustainable steel production, in the production of hydrogen gas under mild hydrothermal conditions (200 – 300 °C, in the presence of carbon dioxide) has been significantly promoted recently [12]. The combination of these industrial needs has promoted scientific efforts toward the characterization of the chemical and physical phenomena of fine powders. However, most of the currently available research is focused on the characterization of the single particle behavior, with little understanding of the interactions between adjacent particles and layers of iron powders.

From a chemical point of view, when exposed to oxidants, metallic iron can react to form stable oxides, such as magnetite (Fe_3O_4) and hematite (Fe_2O_3) based on the fluid dynamic regime, the size of iron particles as well as the availability of the reactants [13], also affecting the macroscopic properties of the resulting flame [14]. The combustion

☆ This article is part of a special issue entitled: 'ISCRE 28' published in Chemical Engineering Journal.

* Corresponding author.
E-mail address: ernesto.salzano@unibo.it (E. Salzano).

https://doi.org/10.1016/j.cej.2025.163164

Available online 28 April 2025
1385-8947/© 2025 The Authors. Published by Elsevier B.V. This is an open access article under the CC BY license (http://creativecommons.org/licenses/by/4.0/).

modes of iron particles in heterogeneous flames have been first investigated based on a single metal particle approach to account for the occurring physical and chemical phenomena and the corresponding rates, including solid-phase kinetic rates, vaporization rate, and molecular diffusion rates of oxidant and thermal energy [15]. Although the achievement of a flame temperature larger than 950 °C can activate the formation of NOx within the exhaust gases, a negligible amount of these species have been detected in iron-fired power plants [3]. According to the thermo-chemical analysis recently reported by Neumann et al. (2024) [5], iron combustion can be modeled as a set of reactions (Equations (1) – (5), forming as an intermediate Fe_zO (Wustite) characterized by a $z \approx 0.95$.

$$Fe + 0.75O_2 \rightarrow 0.5Fe_2O_3 \quad (1)$$

$$Fe + (0.5 \bullet z)O_2 \rightarrow Fe_zO \quad (2)$$

$$Fe_zO + (0.25 \bullet z)O_2 \rightarrow (0.5 \bullet z)Fe_2O_3 \quad (3)$$

$$Fe + 0.66O_2 \rightarrow 0.33Fe_3O_4 \quad (4)$$

$$Fe_3O_4 + 0.25O_2 \rightarrow 1.5Fe_2O_3 \quad (5)$$

Investigations on the heterogeneous reactions in real furnaces reported the formation of FeO as a relevant step into the kinetic mechanism toward the oxidation of iron particles to hematite [15]. In this sense, to properly evaluate the thermo-chemical phenomena of the reactive system, the main thermodynamic properties of the main species potentially involved by the oxidation of Fe are reported in Table 1.

From an experimental perspective, the evaluation of the chemistry of iron oxidation can be investigated by monitoring the evolution along the time of the overall mass and structure of iron particles exposed to an oxidative environment. Following this approach, calorimetric studies and morphological characterization of the microstructure represent powerful tools for kinetic studies of iron oxidation [17]. To this scope, different techniques can be adopted. Among the others, thermogravimetric (TG) analysis under isothermal and non-isothermal conditions in inert or reactive environments is largely considered a benchmark. However, considering the potential impacts of heat transfer phenomena on the investigated system, the utilization of bench-scale apparatuses is highly desirable. This approach can have beneficial effects on the development and validation of models suitable for bulk and multi-particle systems. In addition, it is worth noting that most of the available studies are focused on the flame behavior of microscopic iron particles in suspension in an oxidative medium, typically air, and in the presence of an ignition source [18], with limited literature devoted to the characterization of safety and kinetic aspects in a quiescent regime, especially for non-nano particles [19]. Therefore, a complete understanding of the phenomena ruling the chemistry in a quiescent regime can boost the application of iron particles, providing scientifically-based substrates for the optimized and safe design of storage and transportation systems.

Alternatively, relevant information on the reactivity of iron-based systems can be gathered from an in-depth characterization of the physical and chemical structures of the products. A variety of techniques can be employed for this purpose, including X-ray Diffraction (XRD) for determining crystalline phases, Energy Dispersive Spectroscopy (EDS) for elemental composition, and electron microscopy for detailed surface imaging. Among the other, the use of Scanning Electron Microscopy (SEM) represents a powerful technique to visually evaluate the surface of solid materials. This aspect is particularly relevant if the structural differences between iron oxides are considered. More specifically, SEM provides high-resolution images that allow for a precise evaluation of the surface structure, making it especially useful for detecting subtle morphological changes during oxidation. As a way of example, SEM can reveal whether iron particles undergo swelling or compaction depending on the type of iron oxide formed, which can influence the integrity of the oxide layer and its ability to protect the underlying material from further oxidation. The advantages of SEM lie not only in its ability to provide detailed visual information but also in its relative ease of use and the velocity of analysis compared to other techniques.

For these reasons, calorimetric studies under inert and oxidative environments, at small and bench scales, and initial conditions were performed in this work focusing on the quantification of the heat release rate, the quantification of the apparent kinetic of the main reactions, and the overall reactivity. The structural composition of the obtained products was analyzed and compared with the raw materials investigated in this work. A two-dimensional thermal balance was defined and quantified to represent the phenomena occurring within the bench scale campaign. The combination of the experimental and numerical data collected in this work was employed to develop and validate a kinetic model for the oxidation of iron non-nano particles in a quiescent regime, applicable to real-scale scenarios. Hence, the collected data and resulting models can be of particular interest for the design of robust and safe technological solutions within storage and transportation systems.

Table 1
Summary of the thermodynamic properties of iron and iron oxides, as reported by Chase et al. (1998) [16]. Where ρ: density; T_m: melting temperature; $C_{p,298K}$: heat capacity at 298 K; $\Delta H^{\circ}_{f,298K}$: standard enthalpy of formation; ΔS°_{298K}: standard entropy; LHV: lower heating value.

SPECIES	ρ [KG/M^3]	T_M [°C]	$C_{p,298K}$ [J/MOL/K]	$\Delta H^{\circ}_{f,298K}$ [KJ/MOL]	ΔS°_{298K} [J/MOL/K]	LHV [KJ/G]
FE	7870	1538	25.09	0	27.31	7360
FEO	5740	1377	49.93	−272.04	60.72	2030
FE_3O_4	5180	1590	147.2	−1120.89	145.2	350
FE_2O_3	5260	1565	103.7	−825.5	87.28	0

2. Methodology

In this work, an experimental campaign using the cone calorimeter, as sketched in Fig. 1 and described by ISO 5660 [20], was carried out to characterize iron particles (purity > 99.0 %wt) of median diameters of 74 μm and 450 μm. These values were selected to be representative of possible conditions for the energy production sector [21] and chemical processes [22], respectively. The employed apparatus consists of a radiant heater, having a conical shape, to deliver controlled heat flux to a solid sample placed in a stainless-steel holder 2.5 cm from the heat source. To guarantee the evaluation of metallic particles, samples were stored and prepared under an inert atmosphere before the tests. Once exposed to air, a continuous ignition source (electric spark from a 10 kV high-voltage transformer) was provided. The mass of the sample was monitored by a high-precision load cell. The exhaust gas was gathered under a calibrated exhaust hood, maintaining steady-state conditions and allowing for the quantification of its composition and flow rate. The heat release rate was measured using oxygen consumption calorimetry [23], namely HRR was determined based on the time evolution of the measured oxygen content in the exhaust gas and coefficients deriving from calibrations. Comprehensive calibration ensures accuracy and adherence to international fire testing standards (e.g., ISO 5660 [26] and ASTM E1354 [27]). Additional information on the implemented protocol and features of the constituting elements can be found elsewhere in the literature [2425].

To provide further insights into the reaction mechanism and ongoing phenomena, the standardized methodology typically employed for the experimental campaign involving the cone calorimeter was revised in this work. More specifically, the temperature profile of the sample was measured by K-type thermocouples, placed in the middle of the sample holder (i.e., 5 cm from each lateral wall) at different heights (i.e., 0 cm, 0.5 cm, and 1.0 cm from the bottom) as reported in Fig. 1, once exposed to different external fluxes within 7 – 50 kW/m^2. The evolution of the heat release rate (HRR) and mass gain rate (MGR) was monitored, based

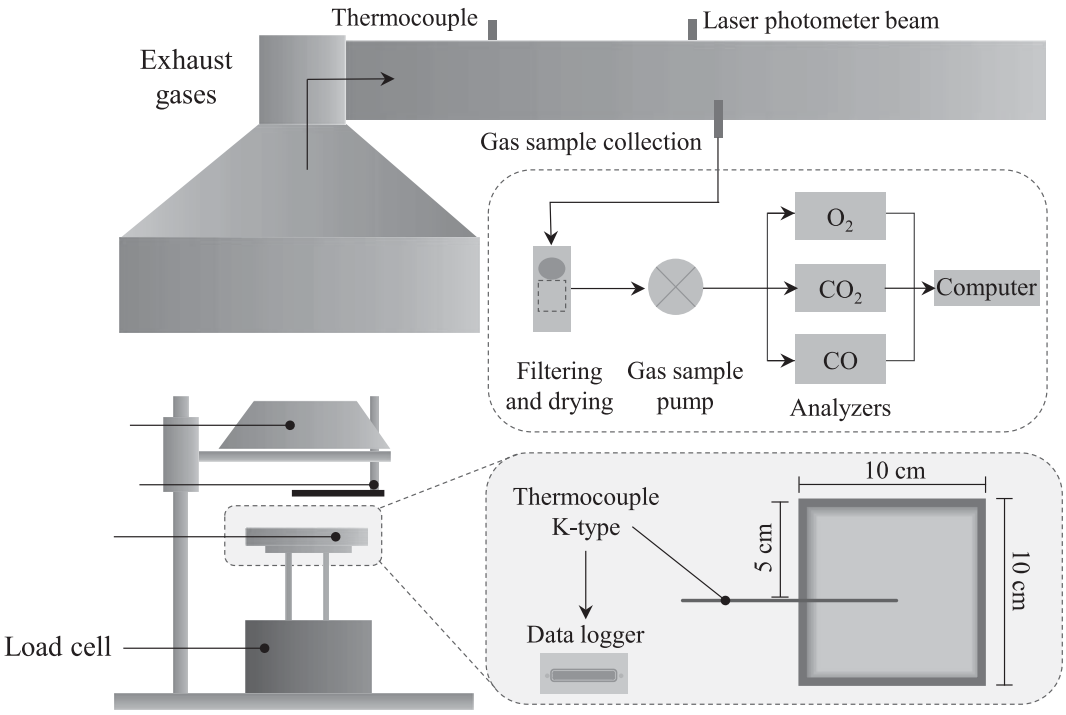

Fig. 1. Detailed experimental configuration of the cone calorimeter equipment.

on direct and indirect (i.e., oxygen consumption method, Equation (6), together with the combustion effectiveness and safety parameters defined elsewhere [28].

$$HRR = \frac{\Delta h_c}{r} \bullet \frac{M_{ox}}{M_{air}} \bullet C \bullet \sqrt{\frac{\Delta P}{T_e}} \bullet \frac{\left(x_{ox}^0 - x_{ox}\right)}{(1 + (b-1)x_{ox}) - bx_{ox}} \tag{6}$$

Where $\frac{\Delta h_c}{r}$ indicates the produced heat per mass of oxygen consumed, M_{ox} and M_{air} are respectively the mass of oxygen and mass of air, x_{ox}^0 and x_{ox} stand for the initial and exhaust molar fraction of oxygen, C and b represent instrumentation constants (*C-factor*), and ΔP and T_e are respectively the exhaust differential pressure and temperature.

Following the experimental campaign, the overall reactivity was evaluated based on the collected measurements and compared with the reaction list mentioned in the previous section (Equations (1) – (5). According to the literature [13,19], the superficial reaction rate r_P of non-nano metal particles can be defined in terms of geometrical properties, stoichiometric coefficients, the initial composition of the gaseous mixture, the kinetic coefficients and mass transport coefficients. However, different formulations can be used based on the assumed rate-determining step. Hence, the measured MGR was compared with r_P calculated in the case of kinetic as the rate-determining step, following the procedure described in the literature [19].

The obtained results were discussed in the view of data gathered through thermogravimetric analysis performed under oxidative (air) and inert (pure nitrogen) environments. In agreement with the kinetic mechanism reported in the previous section, the latter condition was considered as a blank test to evaluate the possible occurrence of physical transformations. All the samples were subjected to thermogravimetric tests under both nitrogen and air atmospheres, with a maximum temperature of 800 °C and a heating rate of 10 °C/min. The maximum temperature was selected considering the Curie point of iron (~768 °C), where significant structural and compositional changes may occur due to the loss of ferromagnetic properties [29], and to ensure consistency with the cone calorimeter tests, where the highest applied heat flux corresponds to approximately 772 °C of the conical heater. Conversely, preliminary tests have highlighted that a heating rate of 10 °C/min represents an excellent trade-off between the accuracy of the obtained data, the representativeness of the observed phenomena, and the effectiveness in the characterization of thermal behavior in small-scale systems.

Scanning electron microscopy (TESCAN MIRA3, SEM microscope) was employed to evaluate the morphology and microstructure of iron particles obtained after thermal treatment. Collected images were compared with homologous data deriving from raw material employed in this work. The analyses were conducted in high vacuum (HV) mode, using an accelerating voltage of 15 kV. Secondary electron (SE) imaging was utilized, with a working distance of approximately 10 mm. Different magnifications were applied depending on the sample under investigation. Wherever possible, both the cross-sections and surface of the samples were analyzed to provide a comprehensive understanding of the iron samples.

Under the assumption of a characteristic time for the heat transfer phenomena involving solid samples significantly smaller than the one for the overall heterogeneous reaction, a homogeneous distribution of sample temperature was considered. This hypothesis will be validated by the comparison of the temperatures measured during each test. Under this impulse, a lumped bi-dimensional model was proposed and tested against experimental data collected in this work. Namely, iron and iron oxide particles were considered as composing a single parallelepipedal block having dimensions 10 x 10 x 1 cm as reported in Fig. 2. More specifically, a heat transfer thermal balance was established (Equation (7) considering the external heat flux (q), depicted by the red arrow and representing the thermal energy emitted by the cone calorimeter onto the sample, the heat flux leaving the system (q_l), indicated by the blue arrow and quantifying the heat dissipated through the external walls of the sample holder (L), and the heat generated (Q_g) by the reactions, reported in black arrows.

$$q_L \bullet L - q \bullet A + Q_g = m \bullet C_p \bullet \frac{dT}{dt} \tag{7}$$

In this sense, it is worth noting that L and A are determined by the geometrical design of the sample holder, q represents an input value for the cone calorimeter tests, imposed as a constant for the whole test, C_p

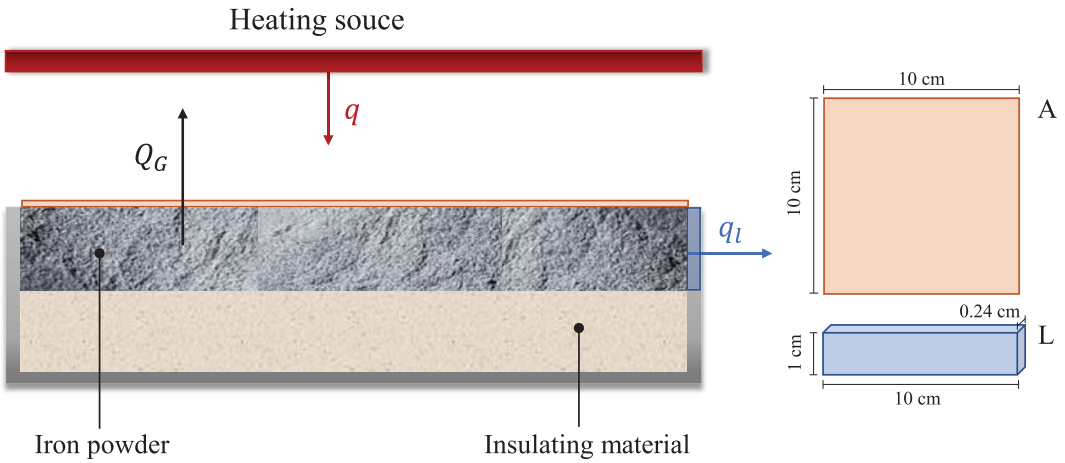

Fig. 2. Schematic representation of thermal contributions during cone calorimeter tests on iron powder.

was calculated at each time interval through the dedicated empirical correlation [30] based on the temperature measured by the thermocouple placed at 0.5 cm from the bottom of the sample holder, m and $\frac{dT}{dt}$ are measured by the load cell and the abovementioned thermocouple, respectively. Eventually, q_L was calculated as the product of the driving force (i.e., the difference between the measured temperatures of the sample and the temperature in the proximity of the sample holder) and the overall heat transfer coefficient (U) accounting for the conduction of iron particles and stainless steel and natural convection. The required parameters and dimensionless correlations suitable for the quantification of these heat transfer coefficients were determined in agreement with the literature [30]. Therefore, Q_g resulted to be the only remaining unknown term within Equation (7). This aspect is particularly significant in the identification of the various reactive steps during the oxidation mechanisms. Indeed, by meticulously evaluating the heat generated, alongside the other contributions, it was possible to support the identification of the reactive steps occurring during the oxidation processes, thereby providing valuable insights into the stability and reactivity of the iron powders under varying thermal conditions. More specifically, the postulated kinetic mechanism was validated by comparing the heat generated resulting from Equation (7) with a theoretical value obtained as the sum of the reaction rates multiplied by the corresponding heat of reactions included within the mechanism.

3. Results and discussion

In this section, the most relevant results obtained by the experimental and theoretical analyses conducted in this work will be presented and discussed. Following the protocol described in the methodological section, measurements from calorimetric approaches will be presented, to identify the key elements and steps within the oxidative process. The gathered information will be used to infer a chain of phenomena characterizing the reactive systems under the investigated conditions. The posed hypothesis will be, then, tested against experimental data deriving from surface analysis and numerical estimations from mass and energy balances.

3.1. Small-scale calorimetry

The time evolutions of the mass collected employing TGA are reported in Fig. 3 for the investigated iron particles under an oxidative environment. For the sake of conciseness, the homologous data obtained in the case of nitrogen atmosphere are not reported since no significant variations in mass are observed along the tests, as can be observed in the supplementary material.

It is worth noting that a difference between the measured mass at the

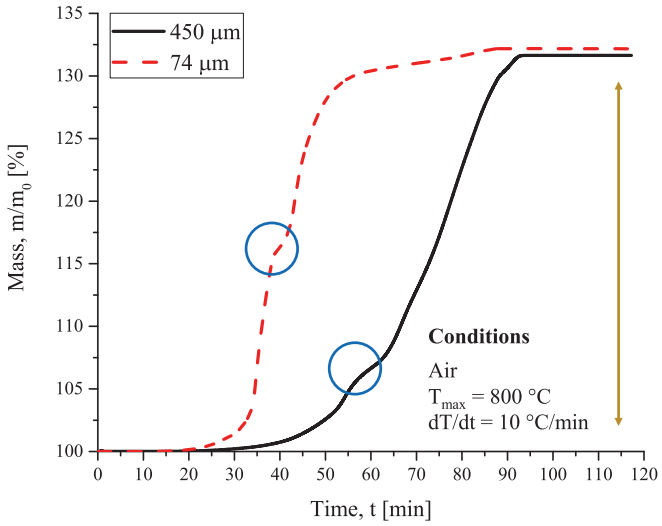

Fig. 3. Time evolution of the mass as collected by thermo-gravimetric analysis of iron particles having different diameters.

end and the beginning of the experiment (Δm_{tot}) of 33 % was observed in both cases, meaning that the overall increase in the sample mass is not affected by the particle diameter once lab scale systems are employed, suggesting the achievement of thermodynamic equilibrium or a complete conversion. Based on the initial composition of the sample and the stoichiometry of the reactions potentially involved, the ratio between the final and initial mass indicates that magnetite and hematite must be present at the end of the test and non-oxidized iron was completely converted. Indeed, a hypothetical complete conversion of Fe exclusively to FeO increases the initial mass by ~ 28 %. Similarly, the complete conversion to Fe_3O_4 or Fe_2O_3 leads to an increase in the initial mass of ~ 38 % and ~ 43 %, respectively. In addition, based on the expected prompt reactivity of FeO under an oxidative atmosphere [15], FeO can be considered as an intermediate species, only. In addition, an abrupt variation in the MGR can be observed in both tests (blue circles in Fig. 3), although occurring at different times (or temperatures). Based on the previous considerations, this trend can be associated with the hypothesis of a two stages reaction mechanism (i.e., Fe → FeO → Fe_3O_4) followed by a three stages mechanism (Fe → FeO → Fe_3O_4 → Fe_2O_3). This assumption is in line with the kinetic mechanism available in the current literature [31]. This assumption will be explored in detail once the measurements from the bench-scale apparatus are discussed, together with the characterization through SEM analyses. The delay in

this variation for the case of larger particles suggests the existence of a regime dominated by oxygen diffusion. A possible time evolution of the chemical composition of single particles is reported in Fig. 4, based on the gathered information.

3.2. Bench-scale calorimetry

For the sake of clarity, only the time evolution of the HRR and mass of the samples obtained by the cone calorimeter tests at 15 kW/m^2 and 35 kW/m^2 for the particle size of 74 μm and 450 μm are reported in Fig. 5 and Fig. 6, respectively.

Three different phases can be distinguished by the evaluation of the HRR and mass trends with the time once the samples having particles of 74 μm are considered. Indeed, regardless of the external heat flux provided to the sample, the tests conducted on the iron particles of 74 μm show an initial peak in HRR which can be attributed to the fast oxidation of the superficial *Fe* to wustite, as confirmed by the initial increase in the sample mass. Once an external heat flux of 15 kW/m^2 is provided to the sample, the peak in HRR is followed by a phase lasting ≈ 30 min (see green arrows in Fig. 6) where an almost constant value of HRR equal to 30 kW/m^2 and a simultaneous linear increase in the sample mass can be observed. The combination of these trends suggests the occurrence of two reactions in series resulting in the following oxidation path: Fe → FeO → Fe_3O_4. This hypothesis is further supported by the comparison of the experimentally determined enthalpy of the reaction (– 1116.8 kJ/mol) and the theoretical value (– 1120.9 kJ/mol), providing a strong validation of the proposed reaction pathway.

When the sample is exposed to an external flux of 35 kW/m^2, the peak in HRR is followed by an almost constant value of sample mass and non-negligible HRR values, indicating the occurrence of disproportionation reaction of wustite ($4FeO \leftrightharpoons Fe_3O_4 + Fe$). During this phase, an almost constant temperature of 850 K [32] was measured by the thermocouples placed inside the intra-particle space. Although the significance of the disproportionation of wustite has been highlighted mostly by previous studies focused on the reduction of iron oxide [33], the occurrence of this reaction has also been proved by *in situ* XRD analysis to be independent of the atmosphere (including inert) in a wide range of temperatures [32]. Bearing in mind the heterogeneous nature of the investigated reactive system, together with the elevated thermal conductivity of iron and iron oxides, the diffusion of oxygen within particles may be assumed as a possible rate-determining step. Therefore, the core of particles can be assumed as *Fe* and the edge as Fe_3O_4 at the end of the second phase, regardless of the external flux provided to the specimen. Conversely, the presence of *FeO* can be affected by the external heat flux provided. The third phase within the HRR trends is characterized by a simultaneous parabolic increase in mass and HRR. Considering the mass transfer limitations on the oxygen diffusion, the observed exothermic phase can be attributed to a superficial reaction, namely the formation of Fe_2O_3 from Fe_3O_4. Hence, a reaction mechanism composed of three stages (i.e., $Fe \rightarrow FeO \rightarrow Fe_3O_4 \rightarrow Fe_2O_3$) can be inferred. At this stage, it is worth mentioning that Δm_{tot} can provide further support to the discussion. Indeed, based on the stoichiometry of reactions, a complete conversion of *Fe* to *FeO*, Fe_3O_4, or Fe_2O_3 would lead to an percentage increase in mass of the sample of about 28.7 %, 43.0 %, and 38.2 %, respectively. In this sense, particles having a diameter of 74 μm exposed to 15 kW/m^2 showed a Δm_{tot} larger than 40 %, meaning that a complete conversion exclusively to *FeO* must be excluded and the conversion of the majority of *Fe* to Fe_3O_4 and Fe_2O_3 can be inferred. Conversely, the presence of *FeO* at the end of the test cannot be excluded once larger external heat fluxes are provided to the sample or larger particles are investigated.

Regardless of the investigated conditions, homogeneous temperatures were measured within the samples during the experimental campaign, supporting the hypothesis reported for the energy balance. Besides, stable phases showing constant temperatures for at least 5 min were observed during the experiments. Therefore, the temperatures measured during the longest stable phase per each experiment (T_{ss}) are presented in Table 2 for various thermal fluxes and diameters analyzed in this work.

As the heat flux increases, T_{ss} significantly increases for both particle sizes. Nevertheless, some discrepancies can be observed once values obtained at the same fluxes are compared. For lower heat fluxes (7 kW/m^2 and 15 kW/m^2), the 74 μm particles reach a significantly higher steady-state temperature than the 450 μm particles. This trend can be only partially attributed to the fact that smaller particles have a larger surface area-to-volume ratio, which leads to faster heating because of the limitations in heat transfer rate by conduction through the walls of the sample holder and convection on the lateral surfaces with respect to internal conduction. Indeed, the achievement of stable values suggests the instauration of a thermal equilibrium. Hence, larger temperatures suggest the occurrence of more exothermic reactions. At higher heat fluxes (35 kW/m^2 and 50 kW/m^2), the difference in steady-state temperature between the two particle sizes becomes smaller, indicating that at high energy input levels, the impact of particle size on temperature diminishes. For the 450 μm particles, there is a noticeable jump in temperature between 15 kW/m^2 (285 °C) and 35 kW/m^2 (554 °C), suggesting that the material may be undergoing a significant physical or chemical change. Similarly, for the 74 μm particles, the temperature stabilizes between 380 °C at 15 kW/m^2 and 575 °C at 35 kW/m^2, with a moderate increase at 50 kW/m^2 to 584 °C. To further support the discussed results, Fig. 7 reports a schematic representation of the experimental system and pictures of the specimen exposed to external heat fluxes.

Fig. 8 represents the profile of the heat generated (Q_g) during the cone calorimeter test on 74 μm iron powder subjected to a heat flux of 15 kW/m^2. The Q_g, normalized by the mass gain rate (MGR), was directly compared to the enthalpy of the reaction of each reactive step, to identify the oxidation mechanism. In the first stage, where magnetite (Fe_3O_4) forms from iron (*Fe*), the Q_g/MGR ratio was equal to − 6.19 kJ/g, which closely aligns with the theoretical value of the standard heat of reaction (ΔH_R°) for the oxidation to magnetite of −6.69 kJ/g [34]. This strong correlation demonstrates that the heat generated during this stage is primarily driven by the oxidation of *Fe* to Fe_3O_4. As the process continues, with the transition from Fe_3O_4 to hematite (Fe_2O_3), the

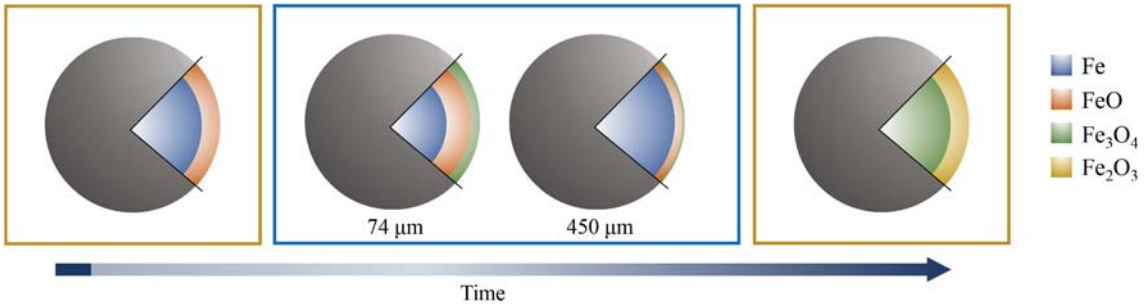

Fig. 4. Schematic representation of the chemical composition of iron particles based on the developed kinetic mechanism.

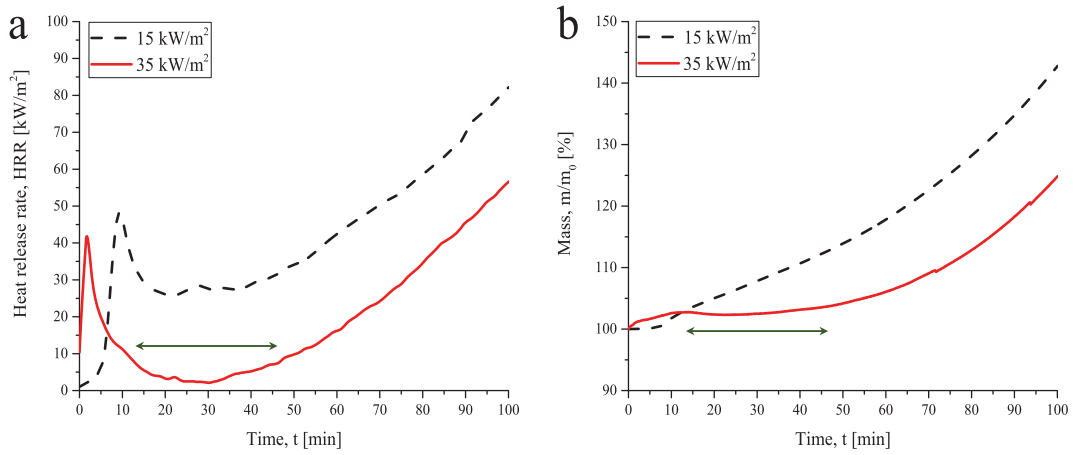

Fig. 5. Time evolution of the heat release rate (a) and sample mass (b) of iron particles of a median diameter of 74 μm exposed to air and different external heat fluxes.

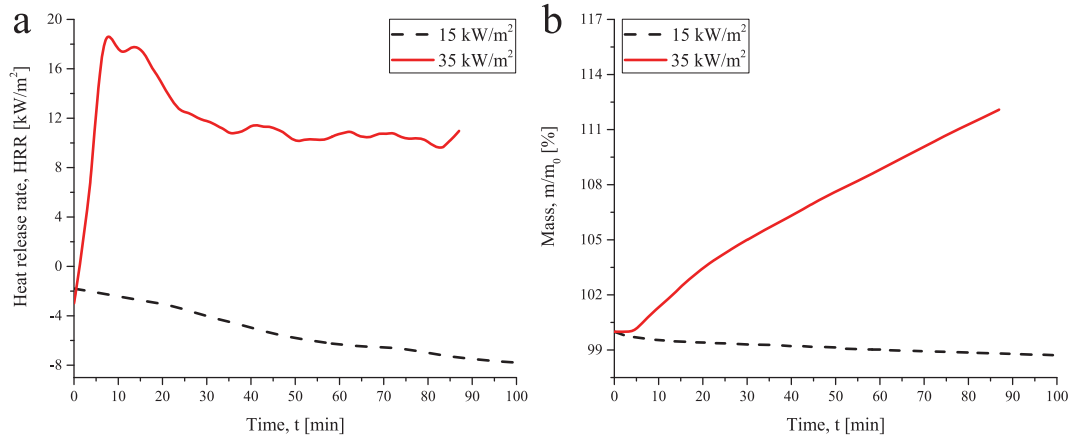

Fig. 6. Time evolution of the heat release rate (a) and sample mass (b) of iron particles of a median diameter of 450 μm exposed to air and different external heat fluxes.

Table 2
Measured temperatures over a stable phase lasting at least 5 min (T_{ss}) for different thermal fluxes and diameters.

Heat Flux [kW/m^2]	Stable temperature over 5 min, T_{ss} [°C]	
	74 μm	450 μm
7	184	121
15	380	285
35	575	554
50	584	594

obtained Q_g/MGR value decreases to −0.49 kJ/g, reflecting the lower values of the standard enthalpy of reaction for this intermediate reaction (−0.51 kJ/g) [34]. In the final step, where complete oxidation to Fe_2O_3 is assumed, the Q_g/MGR reaches −7.84 kJ/g, closely matching the theoretical value of −7.39 kJ/g [34].

3.3. Superficial Scanning of iron samples

In agreement with the postulated mechanism, SEM analysis of the cross-section and surface (Fig. 9) confirmed significant structural differences, further validating the distinct phases of heat generation observed in the profile.

At a heat flux of 35 kW/m^2, the oxidation behavior markedly differs from previous tests, as all oxidation mechanisms occur at significantly accelerated rates. SEM images, reported in Fig. 10, indicate that both the cross-section and surface exhibit comparable characteristics, supporting the observation of a more rapid and uniform oxidation process.

Despite this consistency in surface morphology, it is noteworthy that the oxidation mechanism predominantly develops around the periphery of the particles. As mentioned before, the mass evolution of the sample reveals that not all of the sample has been converted into the final oxidation products. This is evident, as the SEM images, both from the cross-section and surface, suggest a uniform transformation, yet the core of the particles remains incompletely reacted. This phenomenon likely results from diffusion limitations, which restrict the full oxidation of the material under these higher heat flux conditions.

At a heat flux of 35 kW/m^2 for particles having a diameter of 450 μm, the oxidation process displays similar behavior to that observed for smaller particles at 15 kW/m^2. Specifically, according to the obtained profile of the heat generated, the iron undergoes oxidation in two main stages: the initial oxidation to magnetite (Fe_3O_4), followed by further oxidation to Fe_2O_3. These reactions are confirmed through SEM analysis (Fig. 11), particularly when examining the cross-section of the 450 μm sample at 35 kW/m^2, where two distinct zones are evident. For the sake of clarity, blue and red boxes were added to the collected figure to highlight the areas where different structures can be observed. In this sense, it is worth mentioning that the red region represents the area closer to the external heat flux provided by the cone calorimeter and in direct contact with air during the experimental tests.

The blue region reported in Fig. 11 is characterized by larger and more loosely packed particles. Considering the comparison of the

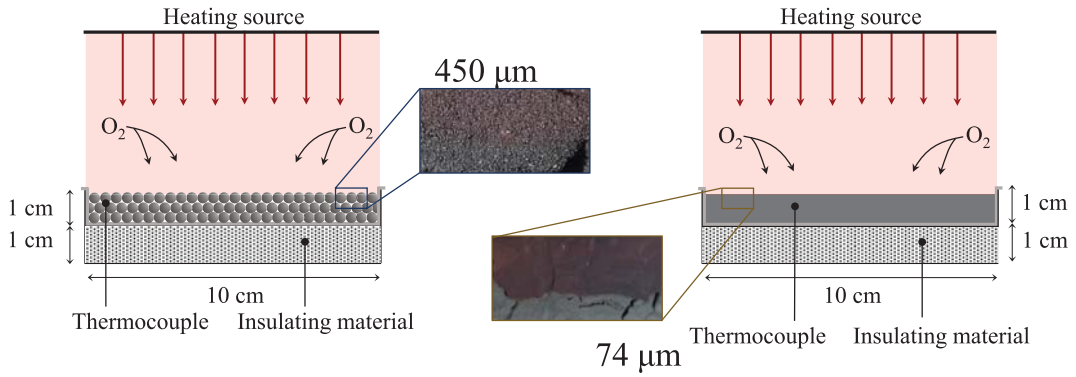

Fig. 7. Schematic representation of the experimental system adopted in this work and visual inspection of the sample structure after tests conducted at 35 kW/m^2 of external heat flux.

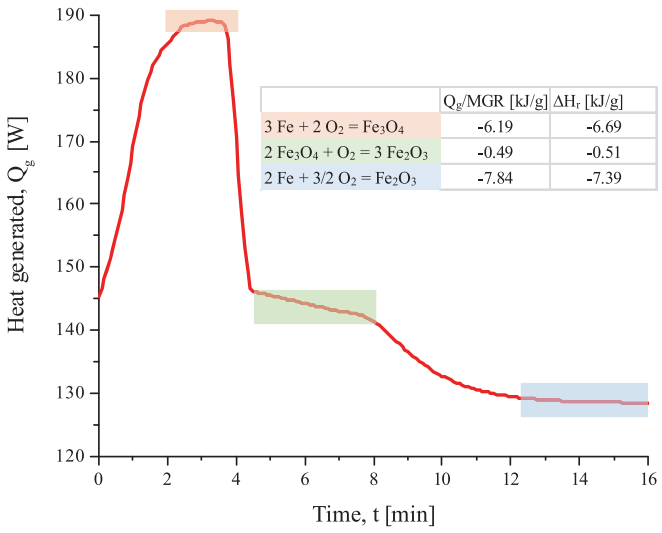

Fig. 8. Heat generated profile over time of a 74 μm iron powder exposed to a 15 kW/m^2 heat flux with the identified reactive steps based on reaction enthalpies.

structural properties of iron oxide particles [35]the predominant phase observed in this region can be identified as magnetite (Fe_3O_4). Meanwhile, the zone within the red rectangle exhibits more densely packed particles. According to the literature [35], this phase corresponds to hematite (Fe_2O_3). Combining this information with the previously proposed kinetic mechanism (i.e., $Fe \rightarrow FeO \rightarrow Fe_3O_4 \rightarrow Fe_2O_3$) and the mass balances, a first stage where the external surface is completely transformed to Fe_3O_4 can be assumed. Hence, interparticle diffusion of oxygen can be assumed as the rate-determining step at this stage for the 450 μm iron powder exposed to an external heat flux of 35 kW/m^2. Afterward, the oxidative step leading to magnetite is followed by further oxidation to hematite, suggesting that the oxidation proceeds downwards in a layer-by-layer mechanism. At this stage, the production of a layer of hematite on the top of the sample (i.e., the surface closer to external heat flux and fresh air) reduces the void fraction and, thus, generates an additional limitation to the intraparticle diffusion of oxygen, hindering the formation of hematite in deeper layers. Therefore, under these assumptions, the intraparticle diffusion can be assumed as the rate-determining step for this second stage of oxidation as confirmed by data from prior studies [36]. In support of these hypotheses, the cross-section surface of the outer layers observed under SEM shows the same characteristics as the red zone, indicating that the surface has fully transitioned to hematite (Fe_2O_3).

4. Conclusions

In this work, an experimental campaign combining small and bench-scale calorimetry was conducted to elucidate the chemistry of the oxidation of iron particles in a quiescent regime under a wide range of conditions. A specific protocol was developed to monitor and combine the most relevant parameters for the characterization of iron oxidation, including the mass gain rate, the heat release rate, and the temperature for different incident heat radiations. Collected data were integrated with surface analysis employing scanning electron microscopy. A bi-dimensional model, merging iron particles in a single solid element that has the effective properties of the investigated reactive systems, was found to accurately describe the system from an energy perspective, meaning that a homogeneous temperature profile can be considered within the iron samples. Conversely, the same approach cannot be successfully adopted for the description of the chemical structure of the sample since single-particle and multi-particle models are required in this case. Hence, the collected data were discussed to enlighten the most relevant aspects potentially characterizing these models. Based on the combination of exothermicity and mass increases along the tests, different steps were distinguished and attributed to the transitions between *Fe, FeO, Fe_3O_4,* and *Fe_2O_3*. An excellent agreement between experimental and theoretical enthalpies of reactions was observed, allowing for the development of suitable kinetic mechanisms. Under this scheme, the rate-determining steps were identified as a function of particle diameter and external heat flux provided to the sample surface. More specifically, the formation of *Fe_2O_3* from *Fe_3O_4* was observed to significantly increase the relevance of intraparticle diffusion of oxygen because of the more compact structure than other oxidized iron species, once large diameters are investigated, exclusively. Under these conditions, a stratified reaction was observed, leading to the distinction of a deeper area rich in non-reacted *Fe_3O_4* by external layers rich in *Fe_2O_3* on the particle surface. Conversely, only small diameters exposed to an external heat flux of 35 kW/m^2 undergo a disproportionation reaction of wustite ($4FeO \leftrightharpoons Fe_3O_4 + Fe$), leading to a stable phase characterized by low intensity of generated heat power during the reaction phase.

The combination of different experimental approaches and theoretical-based evaluations proposed in this work represents an effective protocol for understanding the phenomena characterizing reactive systems. The obtained results allowed for the integration of single-particle models into multi-particle models, closing the gap between fundamental-oriented research and industrial applications. Indeed, the gathered information and the resulting observations represent an essential database for the evaluation of safety and kinetic aspects relevant to the utilization of non-nano metal particles under real case conditions, promoting the safe and optimized utilization of iron powder in several industrial fields, including carbon-free power production.

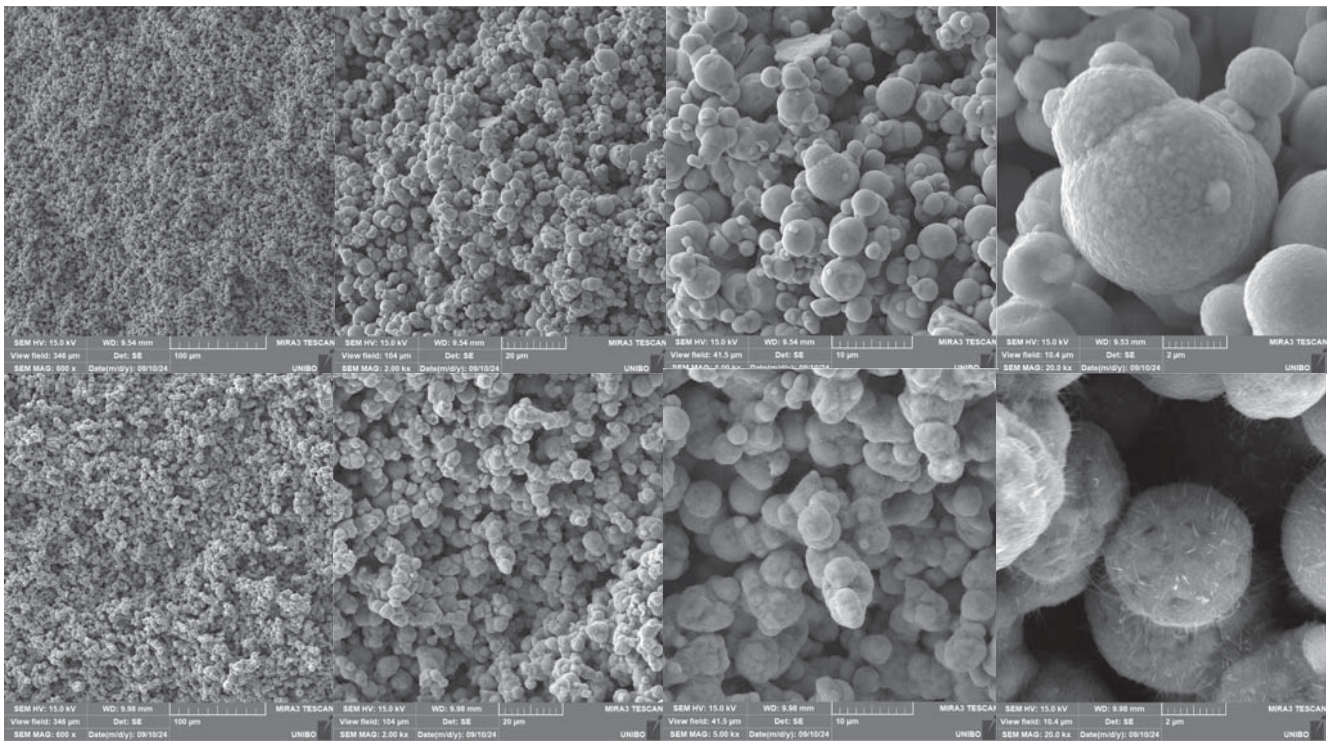

Fig. 9. SEM images of 74 μm iron powder after heating at 15 kW/m^2 from cross-section (top) and surface (bottom) views.

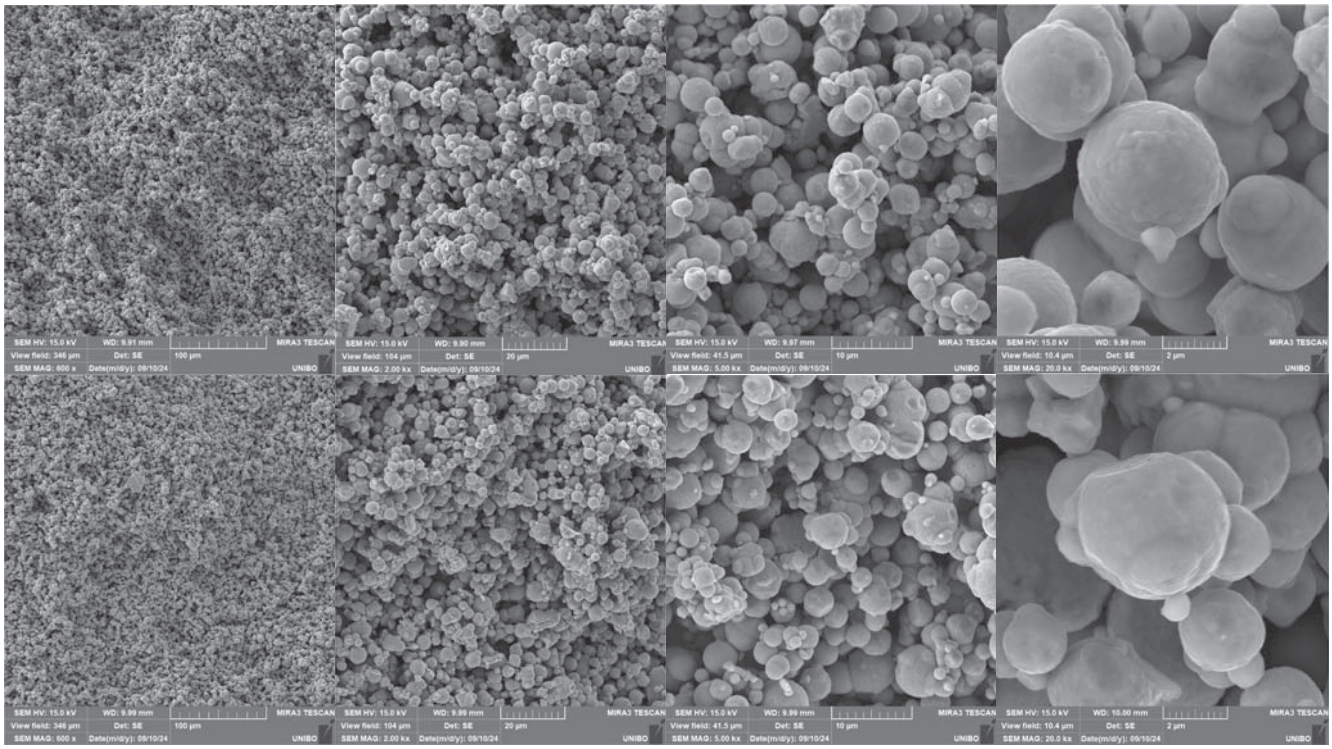

Fig. 10. SEM images of 74 μm iron powder after heating at 35 kW/m^2 from cross-section (top) and surface (bottom) views.

CRediT authorship contribution statement

Benedetta A. De Liso: Writing – original draft, Investigation, Formal analysis, Data curation. **Gianmaria Pio:** Writing – review & editing, Supervision, Software, Methodology. **Clément Chanut:** Writing – review & editing, Validation, Supervision. **Ernesto Salzano:** Writing – review & editing, Supervision, Resources, Project administration.

Declaration of competing interest

The authors declare that they have no known competing financial interests or personal relationships that could have appeared to influence

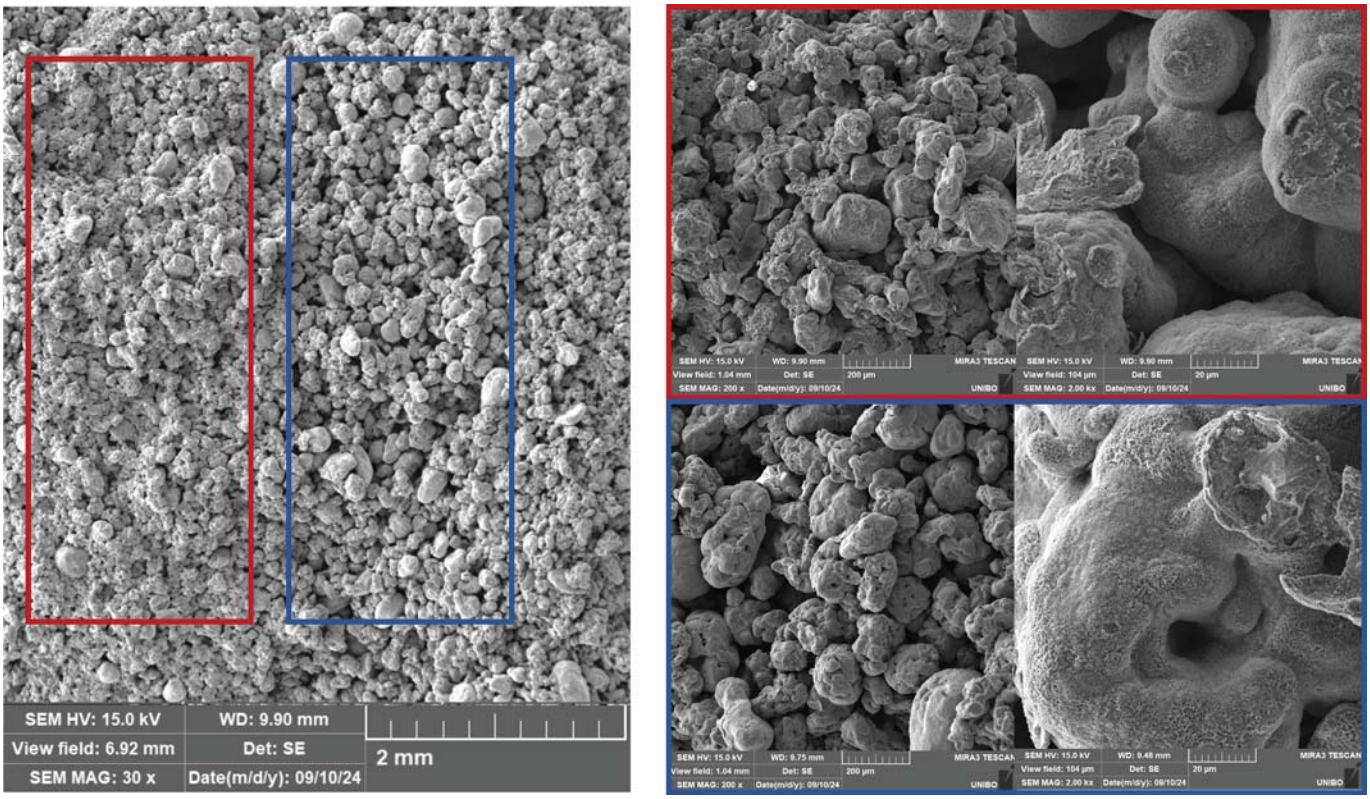

Fig. 11. SEM images of the cross-section of 450 μm iron powder after heating at 35 kW/m^2 at different zoom levels. Two distinct morphological regions are highlighted: the red area, directly exposed to the heat flux, and the blue area, representing the inner, less exposed region.

the work reported in this paper.

Appendix A. Supplementary data

Supplementary data to this article can be found online at https://doi.org/10.1016/j.cej.2025.163164.

Data availability

Data will be made available on request.

References

[1] N. Morlanés, S.P. Katikaneni, S.N. Paglieri, A. Harale, B. Solami, S.M. Sarathy, J. Gascon, A technological roadmap to the ammonia energy economy: Current state and missing technologies, Chem. Eng. J. 408 (2021) 127310, https://doi.org/10.1016/j.cej.2020.127310.

[2] H. Luo, Y. Zeng, D. He, X. Pan, Application of iron-based materials in heterogeneous advanced oxidation processes for wastewater treatment: A review, Chem. Eng. J. 407 (2021) 127191, https://doi.org/10.1016/j.cej.2020.127191.

[3] P. Debiagi, R.C. Rocha, A. Scholtissek, J. Janicka, C. Hasse, Iron as a sustainable chemical carrier of renewable energy: Analysis of opportunities and challenges for retrofitting coal-fired power plants, Renew. Sustain. Energy Rev. 165 (2022) 112579, https://doi.org/10.1016/j.rser.2022.112579.

[4] S. Goroshin, J. Palečka, J.M. Bergthorson, Some fundamental aspects of laminar flames in nonvolatile solid fuel suspensions, Prog. Energy Combust. Sci. 91 (2022), https://doi.org/10.1016/j.pecs.2022.100994.

[5] J. Neumann, Q. Fradet, A. Scholtissek, F. Dammel, U. Riedel, A. Dreizler, C. Hasse, P. Stephan, Thermodynamic assessment of an iron-based circular energy economy for carbon-free power supply, Appl. Energy. 368 (2024), https://doi.org/10.1016/j.apenergy.2024.123476.

[6] J. Janicka, P. Debiagi, A. Scholtissek, A. Dreizler, B. Epple, R. Pawellek, A. Maltsev, C. Hasse, The potential of retrofitting existing coal power plants: A case study for operation with green iron, Appl. Energy. 339 (2023), https://doi.org/10.1016/j.apenergy.2023.120950.

[7] N.I. Villanueva-Martínez, C. Alegre, J. Rubín, R. Mckerracher, C.P. de León, H.A. F. Rodríguez, M.J. Lázaro, Investigation of the properties influencing the deactivation of iron electrodes in iron-air batteries, Electrochim. Acta. 465 (2023) 142964, https://doi.org/10.1016/j.electacta.2023.142964.

[8] Y. Guan, Y. Liu, X. Lin, B. Wang, Q. Lyu, Research Progress and Perspectives of Solid Fuels Chemical Looping Reaction with Fe-Based Oxygen Carriers, Energy Fuel 36 (2022) 13956–13984, https://doi.org/10.1021/acs.energyfuels.2c02802.

[9] J. He, Q. Yang, Z. Song, W. Chang, C. Huang, Y. Zhu, X. Ma, X. Wang, Improving the carbon resistance of iron-based oxygen carrier for hydrogen production via chemical looping steam methane reforming: A review, Fuel 351 (2023) 128864, https://doi.org/10.1016/j.fuel.2023.128864.

[10] Y. Niu, Z. Chi, M. Li, Advancements in biomass gasification research utilizing iron-based oxygen carriers in chemical looping: A review, Mater. Reports Energy. 4 (2024) 100282, https://doi.org/10.1016/j.matre.2024.100282.

[11] V. Vogl, M. Åhman, L.J. Nilsson, Assessment of hydrogen direct reduction for fossil-free steelmaking, J. Clean. Prod. 203 (2018) 736–745, https://doi.org/10.1016/j.jclepro.2018.08.279.

[12] K. Michiels, J. Spooren, V. Meynen, Production of hydrogen gas from water by the oxidation of metallic iron under mild hydrothermal conditions, assisted by in situ formed carbonate ions, Fuel 160 (2015) 205–216, https://doi.org/10.1016/j.fuel.2015.07.061.

[13] I. Glassman, R.A. Yetter, Combustion, 4th ed., Elsevier, San Diego, California, 2008.

[14] S. Goroshin, F.-D. Tang, A.J. Higgins, J.H. Lee, Laminar dust flames in a reduced-gravity environment, Acta Astronaut. 68 (2011) 656–666, https://doi.org/10.1016/j.actaastro.2010.08.038.

[15] J.M. Bergthorson, S. Goroshin, M.J. Soo, P. Julien, J. Palecka, D.L. Frost, D. J. Jarvis, Direct combustion of recyclable metal fuels for zero-carbon heat and power, Appl. Energy. 160 (2015) 368–382, https://doi.org/10.1016/j.apenergy.2015.09.037.

[16] M. jr Chase, C. Davies, J. jr Downey, D. Frurip, R. McDonald, A. Syverud, JANAF Thermochemical Tables, J. Phys. Chem. Ref. Data Suppl. Third Edit (1998) 548.

[17] F. Cerciello, A. Fabozzi, C. Yannakis, S. Schmitt, O. Narin, V. Scherer, O. Senneca, Kinetics of iron reduction upon reduction/oxidation cycles, Int. J. Hydrogen Energy. 65 (2024) 337–347, https://doi.org/10.1016/j.ijhydene.2024.04.008.

[18] F.-D. Tang, S. Goroshin, A.J. Higgins, Modes of particle combustion in iron dust flames, Proc. Combust. Inst. 33 (2011) 1975–1982, https://doi.org/10.1016/j.proci.2010.06.088.

[19] E. Danzi, G. Pio, L. Marmo, E. Salzano, The explosion of non-nano iron dust suspension in the 20-l spherical bomb, J. Loss Prev. Process Ind. 71 (2021) 104447, https://doi.org/10.1016/j.jlp.2021.104447.

[20] BS ISO 5660-1 : 2015 + A1 : 2019 — Tracked Changes Reaction-to-fire tests — Heat release , smoke production and mass loss rate, (2019).

[21] M. Sohrabi, B. Ghobadian, G. Najafi, W. Prasidha, M. Baigmohammadi, P. de Goey, Experimental and Statistical Analysis of Iron Powder for Green Heat Production, Sustainability. 16 (2024) 9416, https://doi.org/10.3390/su16219416.

[22] T. Xu, X. Wang, B. Xiao, H. Zhao, W. Liu, Optimisation of syngas production from a novel two-step chemical looping reforming process using Fe-dolomite as oxygen

carriers, Fuel Process. Technol. 228 (2022) 107169, https://doi.org/10.1016/j.fuproc.2022.107169.
[23] O. Willstrand, M. Pushp, H. Ingason, D. Brandell, Uncertainties in the use of oxygen consumption calorimetry for heat release measurements in lithium-ion battery fires, Fire Saf. J. 143 (2024) 104078, https://doi.org/10.1016/j.firesaf.2023.104078.
[24] B.A. De Liso, G. Pio, E. Salzano, Fire behaviour of liquid solvents for energy storage applications, Process Saf. Environ. Prot. 188 (2024) 726–734, https://doi.org/10.1016/j.psep.2024.05.153.
[25] B.A. De Liso, G. Pio, E. Salzano, Small scale pool fires: The case of toluene, J. Loss Prev. Process Ind. 92 (2024), https://doi.org/10.1016/j.jlp.2024.105430.
[26] ISO 5660, ISO 5660-1: 2019. Reaction-to-fire tests. Heat release, smoke production and mass loss rate Heat release rate (cone calorimeter method) and smoke production rate (dynamic measurement), 2019.
[27] ASTM E1354, ASTM E1354-23 - Standard Test Method for Heat and Visible Smoke Release Rates for Materials and Products Using an Oxygen Consumption Calorimeter, 2023.
[28] M. Tahmid Islam, J.L. Klinger, M. Toufiq Reza, Evaluating combustion characteristics and combustion kinetics of corn stover-derived hydrochars by cone calorimeter, Chem. Eng. J. 452 (2023) 139419, https://doi.org/10.1016/j.cej.2022.139419.
[29] Y.C. Liu, F. Sommer, E.J. Mittemeijer, Calibration of the differential dilatometric measurement signal upon heating and cooling; Thermal expansion of pure iron, Thermochim. Acta. 413 (2004) 215–225, https://doi.org/10.1016/j.tca.2003.10.005.
[30] R.H. Perry, B.E. Poling, G.H. Thomson, D.G. Friend, R.L. Rowley, W.V. Wilding, Perry's Chemical Engineers' Handbook - Section 2: Physical and Chemical Data, 8th ed., United State of America, 2007. https://doi.org/10.1036/0071511253.
[31] E.N. Lysenko, A.P. Surzhikov, S.P. Zhuravkov, V.A. Vlasov, A.V. Pustovalov, N. A. Yavorovsky, The oxidation kinetics study of ultrafine iron powders by thermogravimetric analysis, J. Therm. Anal. Calorim. 115 (2014) 1447–1452, https://doi.org/10.1007/s10973-013-3456-x.
[32] W.K. Jozwiak, E. Kaczmarek, T.P. Maniecki, W. Ignaczak, W. Maniukiewicz, Reduction behavior of iron oxides in hydrogen and carbon monoxide atmospheres, Appl. Catal. A Gen. 326 (2007) 17–27, https://doi.org/10.1016/j.apcata.2007.03.021.
[33] Q. Fradet, M. Kurnatowska, U. Riedel, Thermochemical reduction of iron oxide powders with hydrogen: Review of selected thermal analysis studies, Thermochim. Acta. 726 (2023) 179552, https://doi.org/10.1016/j.tca.2023.179552.
[34] NIST, NIST Chemistry WebBook 69, National Institute of Standards and Technology, (2024).
[35] K.Q. Jabbar, A.A. Barzinjy, S.M. Hamad, Iron oxide nanoparticles: Preparation methods, functions, adsorption and coagulation/flocculation in wastewater treatment, Environ. Nanotechnology, Monit. Manag. 17 (2022), https://doi.org/10.1016/j.enmm.2022.100661.
[36] H. Larsson, T. Jonsson, R. Naraghi, Y. Gong, R.C. Reed, J. Ågren, Oxidation of iron at 600 °C – experiments and simulations, Mater. Corros. 68 (2017) 133–142, https://doi.org/10.1002/maco.201508781.